PROBING SPACE-TIME EVOLUTION AND FINAL-STATE INTERACTIONS IN RELATIVISTIC HEAVY-ION COLLISIONS VIA FEMTOSCOPY

Hanna Zbroszczyk

Warsaw University of Technology, Faculty of Physics
Koszykowa 75, 00-662 Warsaw, Poland

Received 31 March 2026, accepted 9 April 2026, published online 28 May 2026

Femtoscopy, historically associated with Hanbury-Brown–Twiss (HBT) interferometry, has evolved into a precision tool for investigating the space-time structure of particle-emitting sources created in high-energy collisions. While the term HBT is often used, it captures only a subset of the broader class of femtoscopic correlation techniques based on quantum-statistical correlations. This review provides a systematic overview of femtoscopic measurements across a broad range of collision energies and system sizes. We explore the "sizes" of homogeneity regions through detailed energy scans, spanning from the low-energy regime of HADES to the highest energies of the RHIC Beam Energy Scan and the LHC. We examine the system-size dependence of these regions, including the intermediate regime of p–Pb collisions at the LHC, which serves as a bridge between elementary p–p and dense A–A systems, while highlighting the breakdown of universal multiplicity scaling due to initial-state geometric effects. Furthermore, we discuss non-identical particle correlations, such as π–K, as a unique probe of relative space-time emission asymmetries, providing independent evidence for collective transverse expansion. The review also addresses "interaction femtoscopy" exploiting the sensitivity of correlation functions to final-state interactions in order to extract scattering parameters for (anti)protons, Λ hyperons, and light nuclei. These measurements impose important constraints on hyperon–nucleon and three-body interactions, supplying essential input for chiral effective field theory and the equation of state of dense nuclear matter, with significant implications for the internal structure of neutron stars.

DOI:10.5506/APhysPolB.57.6-A9

1. Introduction

Femtoscopy [1] is an experimental technique used to determine the space-time characteristics of a particle-emitting source via momentum-space correlations [2–5]. Originally developed in radio-astronomy to measure the an-

gular diameters of stars [6, 7], it was later adapted to subatomic physics to probe the regions of homogeneity at kinetic freeze-out — the stage at which particles decouple from the system and cease to interact [8–11].

In high-energy nuclear collisions [5, 12–16], the two-particle correlation function $C(p_1, p_2)$ is typically defined as the ratio of the joint probability of detecting two particles with momenta p_1 and p_2 to the product of their single-particle probabilities. Experimentally, it is constructed as

$$C(q) = \frac{A(q)}{B(q)}\,, \tag{1}$$

where q denotes the relative momentum of the pair, $A(q)$ is the distribution of particle pairs from the same event, and $B(q)$ is a reference distribution obtained using event-mixing techniques.

The correlation function is related to the spatial distribution of emission points through the Koonin–Pratt equation [17, 18]

$$C(q) = \int S(r, K)\,|\Psi(r, q)|^2\,\mathrm{d}^3 r\,, \tag{2}$$

where $S(r, K)$ is the source function describing the distribution of relative emission distances r in the pair rest frame, and $\Psi(r, q)$ is the two-particle wavefunction. The latter incorporates both quantum statistics (Bose–Einstein or Fermi–Dirac) and final-state interactions (FSI), including Coulomb and strong interactions.

For identical particles, the one-dimensional correlation function is often parameterized in terms of the invariant momentum difference $q_{\mathrm{inv}} = \sqrt{(p_1 - p_2)^2 - (E_1 - E_2)^2}$, allowing for the extraction of an invariant radius R_{inv}

$$C(q_{\mathrm{inv}}) = 1 + \lambda \exp\left(-q_{\mathrm{inv}}^2 R_{\mathrm{inv}}^2\right)\,, \tag{3}$$

where λ is the chaoticity parameter, accounting for partial coherence of the source and contributions from resonance decays.

In three dimensions, the relative momentum is decomposed in the Bertsch–Pratt "out–side–long" (o–s–l) coordinate system [19]. In the Longitudinal Co-Moving System (LCMS), the correlation function is parameterized as

$$C(q_{\mathrm{out}}, q_{\mathrm{side}}, q_{\mathrm{long}}) = 1 + \lambda \exp\left(-q_{\mathrm{out}}^2 R_{\mathrm{out}}^2 - q_{\mathrm{side}}^2 R_{\mathrm{side}}^2 - q_{\mathrm{long}}^2 R_{\mathrm{long}}^2\right)\,. \tag{4}$$

Here, R_{long} is sensitive to the longitudinal expansion and system lifetime, R_{side} reflects the transverse geometric size, and R_{out} depends on both the spatial extent and the duration of particle emission. These parameterizations form the basis for the physical interpretation of femtoscopic measurements discussed in the following sections.

2. Sizes femtoscopy

2.1. Energy Scan including top energies

The RHIC Beam Energy Scan (BES) program has enabled a systematic investigation of the excitation functions of HBT radii over more than two orders of magnitude in center-of-mass energy. Measurements from Au+Au collisions at $\sqrt{s_{NN}} = 7.7$–200 GeV from the STAR experiment, complemented by HADES' ones (see Fig. 1) provide essential insight into the evolution of the fireball created in relativistic heavy-ion collisions.

The energy dependence of the radii, particularly for central collisions at low transverse momentum, exhibits a remarkably smooth behavior. Both R_{side} and R_{out} show only modest variation across the BES range, whereas R_{long} increases steadily with beam energy. This growth of R_{long} is commonly interpreted as reflecting an increase in the total lifetime of the system, indicating that the matter remains longer in the deconfined and/or mixed phases at higher energies. The ratio $R_{\text{out}}/R_{\text{side}}$, which was predicted to rise significantly in the presence of a first-order phase transition due to prolonged emission duration, remains approximately constant. This observation imposes strong constraints on the equation of state and the space-time dynamics of the expansion.

The transverse mass (m_{T}) dependence of HBT radii is a well-established signature of collective flow. Across the full BES energy range, the radii decrease with increasing m_{T}, reflecting strong space-momentum correlations. At higher m_{T}, femtoscopy probes smaller homogeneity regions rather than the full geometric size of the system. The similarity of the m_{T} slopes seen in Fig. 2 across different energies suggests that the underlying expansion dynamics, driven by pressure gradients, are largely universal from $\sqrt{s_{NN}} = 7.7$ GeV up to the top RHIC energies.

A particularly powerful extension of these studies is the azimuthally differential HBT analysis, where the radii are measured with respect to the reaction plane. This enables the extraction of the freeze-out eccentricity ϵ_{F}. While the initial-state eccentricity ϵ_{PP} is typically out-of-plane extended, the system undergoes stronger in-plane expansion. The extracted ϵ_{F} (see Fig. 3) decreases monotonically with increasing beam energy, indicating that higher energies lead to longer lifetimes and stronger pressure gradients, allowing the system to evolve toward a more isotropic shape. The absence of any non-monotonic behavior disfavors scenarios predicting a strong softening of the equation of state. See Fig. 4 for more details.

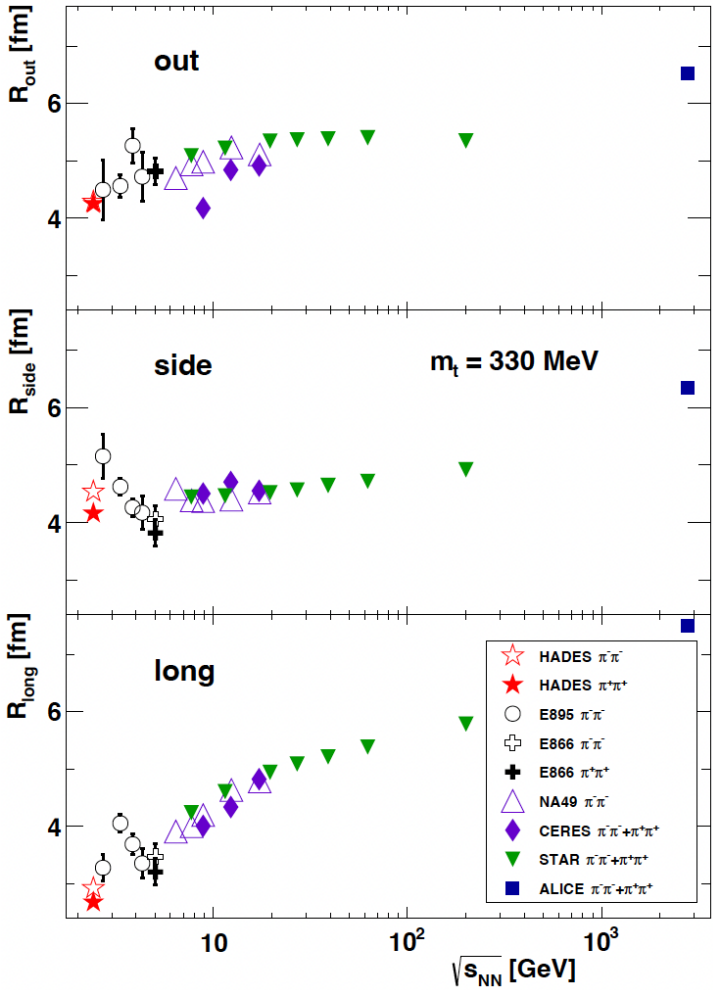

Fig. 1. Excitation functions of the source radii $R_{\rm out}$ (upper panel), $R_{\rm side}$ (middle panel), and $R_{\rm long}$ (lower panel) are shown for azimuthally integrated correlation functions of identical pion pairs with a transverse mass of 330 MeV in central (0-10%) Au+Au and Pb+Pb collisions. The data points correspond to different experiments: squares denote ALICE measurements at the LHC, filled triangles represent STAR results at RHIC, diamonds correspond to CERES data at the SPS, open triangles indicate NA49 results at the SPS, open circles represent E895 measurements at the AGS, and open (filled) crosses correspond to E866 data at the AGS. The HADES results at SIS18 for charged pion pairs are shown as open (filled) stars. Statistical uncertainties are indicated by the error bars; where not visible, they are smaller than the marker size [20].

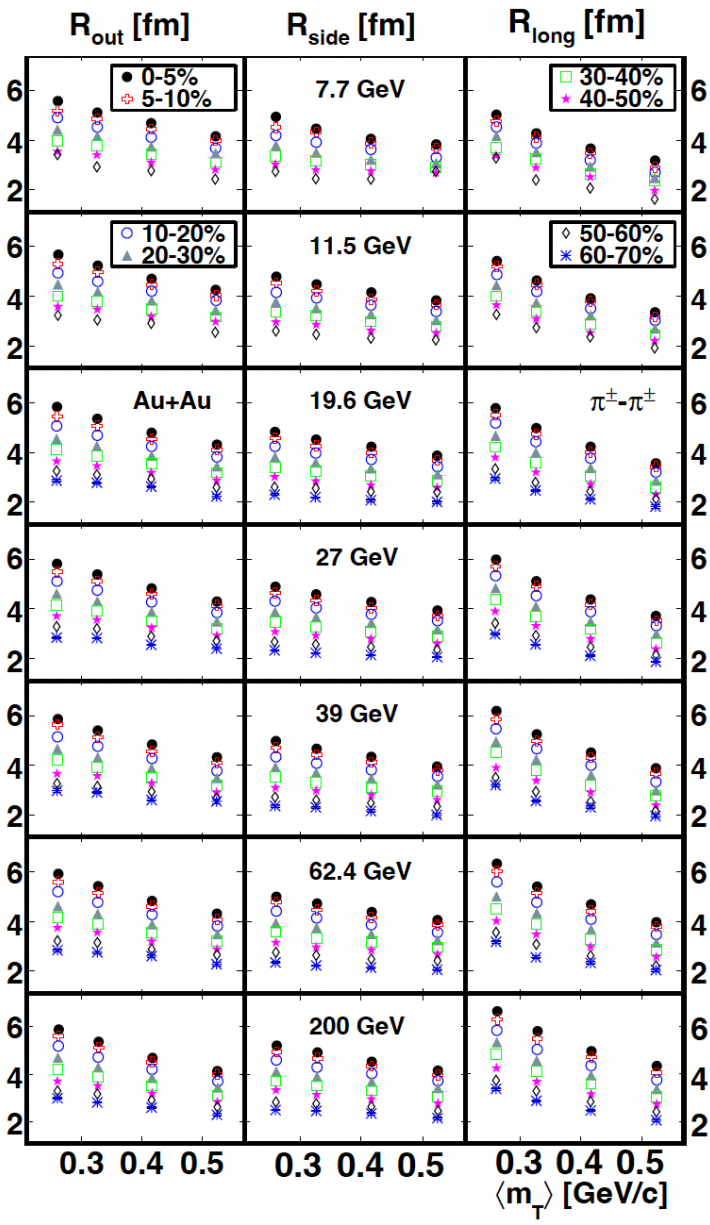

Fig. 2. The $\langle m_{\mathrm{T}} \rangle$ dependence of R_{out}, R_{side}, and R_{long} is shown for each collision energy and for multiple centrality classes. The quoted uncertainties are statistical only. For $\sqrt{s_{NN}} = 7.7$ and 11.5 GeV, the results for the 60–70% centrality class are not included due to insufficient statistics [21].

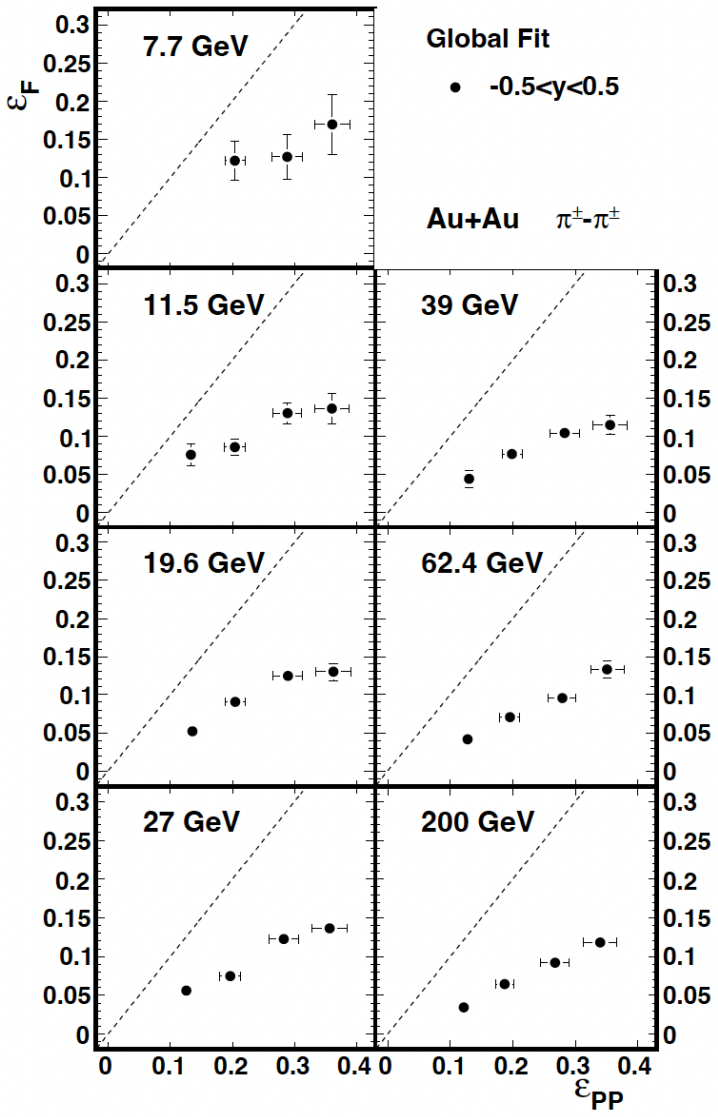

Fig. 3. The eccentricity at kinetic freeze-out, ϵ_{F}, is shown as a function of the initial eccentricity with respect to the participant plane, ϵ_{PP}, at midrapidity. All results correspond to $\langle k_{\mathrm{T}} \rangle \approx 0.31$ GeV/c. The error bars represent statistical uncertainties only. The solid line has a slope of unity, indicating no evolution of the system shape. Data points located further below this line correspond to systems that evolve toward a more isotropic (round) configuration [21].

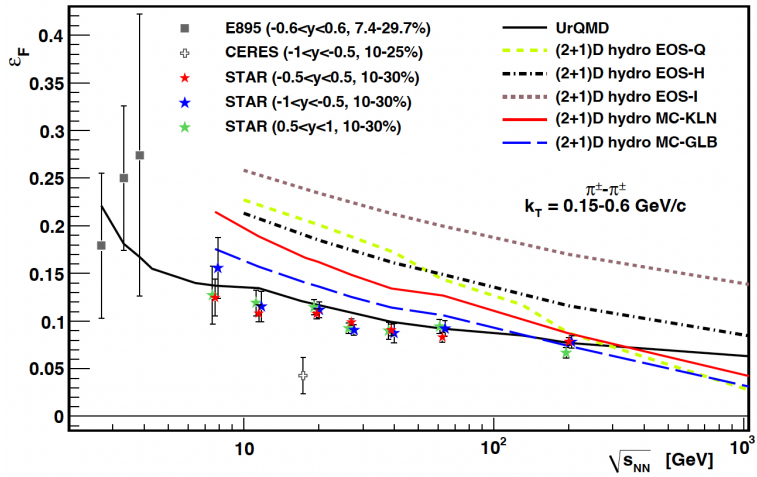

Fig. 4. The dependence of the pion kinetic freeze-out eccentricity on collision energy is shown for mid-central Au+Au collisions (E895, STAR) and Pb+Au collisions (CERES), evaluated in three rapidity intervals at $\langle k_{\mathrm{T}} \rangle \approx 0.31$ GeV/c. For clarity, the STAR data points at forward and backward rapidities are slightly offset. Error bars represent statistical uncertainties only. Predictions from several (2+1)D hydrodynamic models, as well as UrQMD calculations, are included, with model centralities matched to the experimental selections. The overall trend is consistent with a monotonic decrease of the freeze-out eccentricity with increasing beam energy [21].

2.2. Low energies

In the low-energy regime explored by the HADES experiment at SIS18 ($\sqrt{s_{NN}} \approx 2.4$ GeV), the properties of the emitting source are governed by different mechanisms, including strong baryon stopping and the influence of the Coulomb field of the charged fireball.

The m_{T} dependence of pion radii presented in Fig. 5 at these energies exhibits a clear charge-dependent splitting. Radii extracted from $\pi^-\pi^-$ pairs are systematically larger than those from $\pi^+\pi^+$ pairs. This effect is naturally explained by the net positive charge of the system: the Coulomb field attracts π^- and repels π^+, thereby modifying their emission trajectories and effective homogeneity lengths. After correcting for Coulomb effects, the extracted radii follow the expected scaling with the cube root of the number of participants, $A_{\mathrm{part}}^{1/3}$, consistent with trends observed at higher energies.

The excitation function of HBT radii toward low energies shows that R_{long} decreases continuously with decreasing beam energy, reaching its minimum in the SIS energy range. This behavior reflects the shorter lifetime of the system at low energies, where the available energy for expansion is

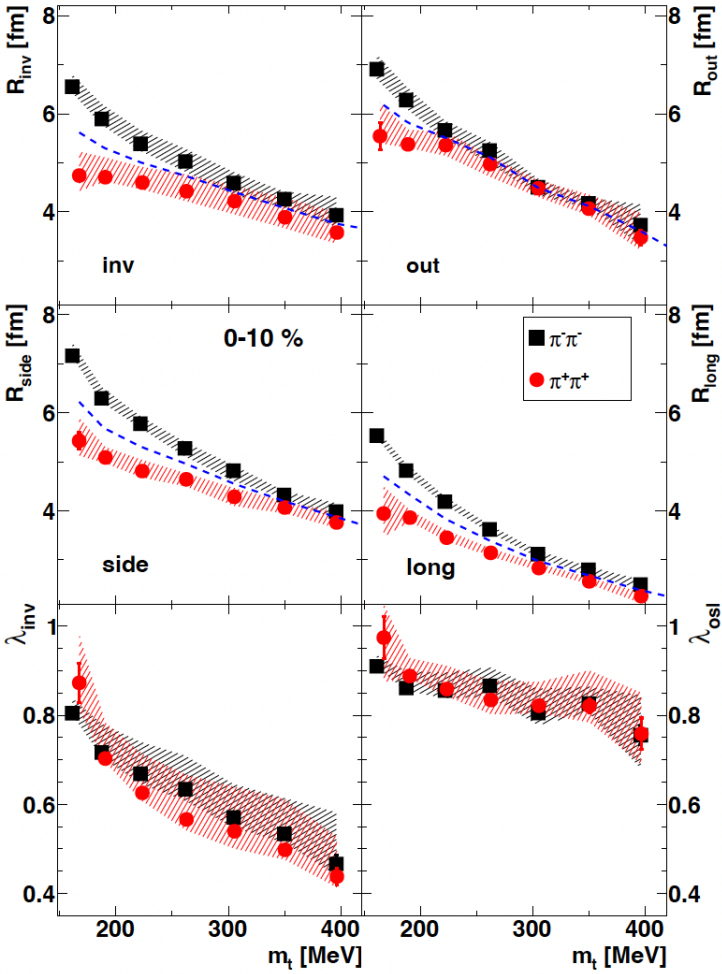

Fig. 5. Source radii as a function of the pair transverse mass, m_{T}, are shown for central (0–10%) Au+Au collisions at 1.23 A GeV. The corresponding transverse momentum range of the pair, $p_{\mathrm{T},12}$, spans 100–800 MeV/c. The upper left, upper right, middle left, and middle right panels present the invariant, "out", "side", and "long" radii, respectively. The lower left and lower right panels display the corresponding λ parameters obtained from fits to the one- and three-dimensional correlation functions. Black squares (red circles) denote pairs of negative (positive) pions. The blue dashed curves represent the reconstructed radii for neutral pion pairs. The error bars indicate statistical uncertainties, while hatched bands correspond to systematic uncertainties [20].

limited. Azimuthally sensitive analyses further indicate that the freeze-out source remains significantly out-of-plane extended, with the tilt angle of the emission ellipsoid decreasing toward more central collisions. These results provide an essential baseline for understanding the emergence of collective behavior as the system evolves from hadronic matter toward the quark–gluon plasma.

2.3. System dependence

The comparison between small systems (such as p+p) and large systems (such as Pb+Pb) offers a stringent test of the universality of femtoscopic scaling.

At LHC energies, measurements in p+p collisions at $\sqrt{s} = 0.9$ and 7 TeV reveal further deviations from simple scaling behavior. Although the radii continue to grow with multiplicity, the slope of this dependence changes. Moreover, at high multiplicity, a pronounced k_{T} dependence emerges, consistent with collective-like behavior. This suggests that even small systems can develop significant space-momentum correlations when sufficiently high-energy densities are reached. The interpretation is complicated by non-femtoscopic correlations, such as mini-jets, which dominate at high k_{T} and low multiplicity and require careful modeling.

p–Pb collisions at $\sqrt{s_{NN}} = 5.02$ TeV provide an important intermediate system between p–p and A–A collisions. Measurements show that the radii increase with event multiplicity and decrease with pair transverse momentum, mirroring the trends observed in heavy-ion systems. At a fixed multiplicity, the radii in p–Pb are typically 10–20% larger than in p–p, yet remain smaller than in A–A collisions.

These results in Fig. 6 highlight the breaking of "universal" scaling of HBT radii with $\langle \mathrm{d}N_{\mathrm{ch}}/\mathrm{d}\eta \rangle^{1/3}$. While both p–p and A–A data exhibit approximately linear scaling, they follow distinct trends. The p–Pb system occupies an intermediate position between these regimes, indicating that the final multiplicity alone does not uniquely determine the freeze-out geometry. Instead, the initial spatial configuration plays a crucial role. Additionally, the emission source in p–Pb is found to be non-Gaussian, often better described by an exponential — Gaussian — exponential (EGE) form, similar to observations in p+p collisions, suggesting contributions from resonance decays and soft parton fragmentation.

2.4. Nonidentical particle correlations

While identical-particle femtoscopy provides access to the size of homogeneity regions, nonidentical particle correlations (*e.g.*, π–K, π–p) offer unique sensitivity to relative space-time emission asymmetries between dif-

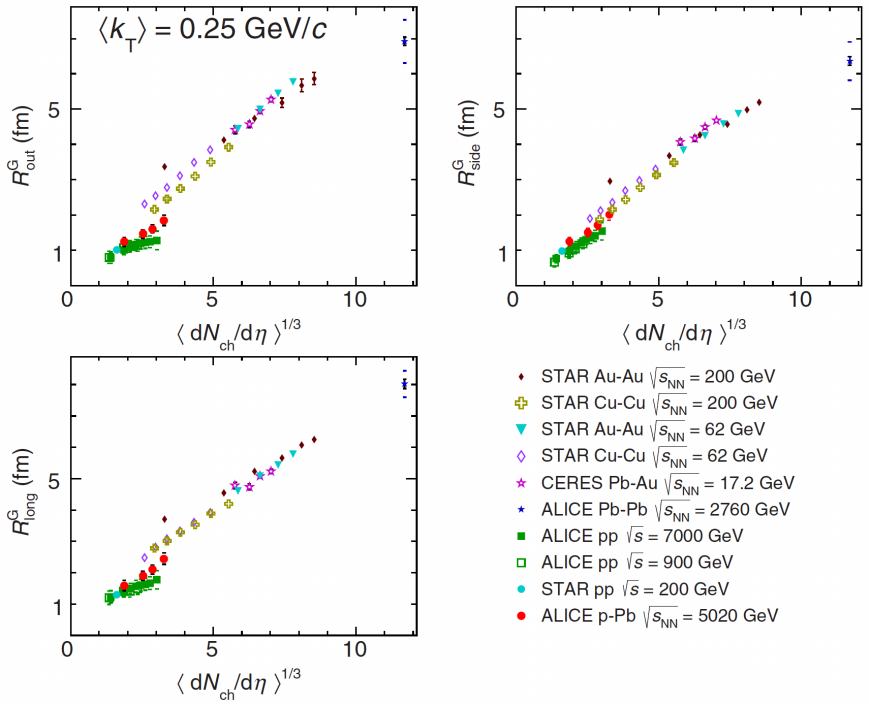

Fig. 6. Comparison of Gaussian femtoscopic radii as a function of the measured charged-particle multiplicity density for various collision systems and energies, as reported by the CERES, STAR, PHENIX, and ALICE experiments [22].

ferent particle species. These asymmetries arise from differences in average emission times and spatial emission points, reflecting the interplay of collective dynamics and hadronic processes.

Measurements of π–K correlations in central Au+Au collisions at $\sqrt{s_{NN}} =$ 130 GeV by the STAR Collaboration employ a double-ratio technique. By constructing the ratio C_+/C_- based on the sign of the projection of the relative momentum onto the pair velocity direction ($k^*_{\rm out}$), one can directly probe emission asymmetries. In the absence of such asymmetries, this ratio would be unity, experimentally, however, a clear deviation is observed at low relative momentum.

The extracted shift, $\langle \Delta r^*_{\rm out} \rangle \approx -5.6$ fm in the pair rest frame, indicates that pions are emitted, on average, closer to the center of the system and/or at later times than kaons. This behavior presented in Fig. 7 is naturally explained by collective transverse expansion. Due to their lower mass, pions exhibit a larger thermal velocity spread, effectively shifting their emission region inward for a given pair velocity. In addition, resonance decays con-

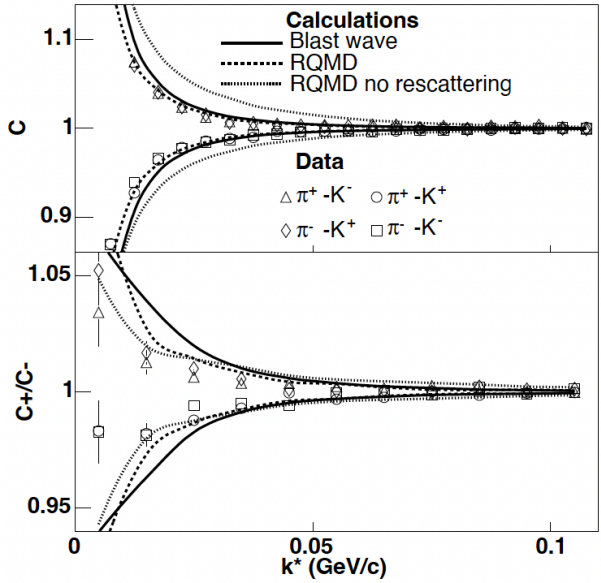

Fig. 7. Comparison of experimental data and model calculations. The upper panel shows the correlation function $C(k^*)$, while the lower panel presents the ratio C_+/C_- as a function of the sign of $k^*_{\rm out}$ [23].

tribute to a delayed emission of pions. These findings provide independent and robust evidence for the presence of collective transverse flow in heavy-ion collisions, consistent with a hydrodynamic description of the system evolution.

3. Interaction femtoscopy

3.1. Proton–proton

Interaction femtoscopy with protons and antiprotons provides a stringent test of CPT symmetry and the properties of the nuclear force. By comparing p–p and $\bar{p}$–$\bar{p}$ correlations in Au+Au collisions at RHIC, the interaction between antiprotons has been directly accessed for the first time.

The correlation functions presented in Fig. 8 for both p–p and $\bar{p}$–$\bar{p}$ pairs exhibit a characteristic maximum at $k^* \approx 0.02$ GeV/c. This enhancement arises from the attractive singlet s-wave strong interaction, which partially compensates for the Coulomb repulsion between identically charged baryons. The ratio of the p–p to $\bar{p}$–$\bar{p}$ correlation functions is found to be consistent with unity over nearly the entire relative momentum range.

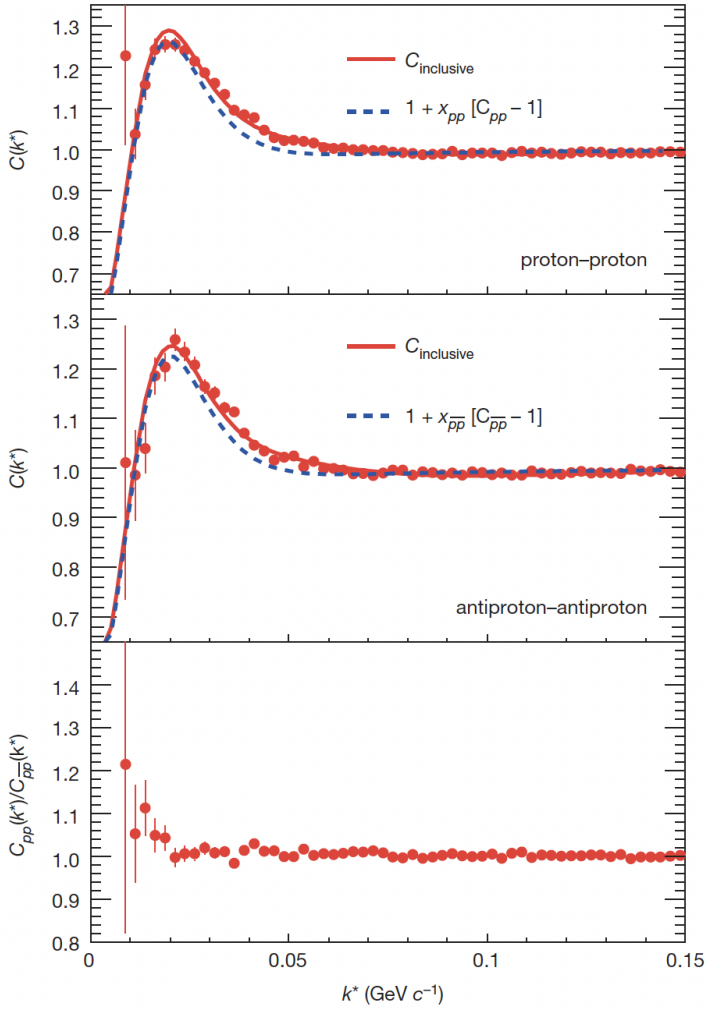

Fig. 8. Correlation functions for proton–proton pairs (top panel), antiproton–antiproton pairs (middle panel), and their ratio (bottom panel). The uncertainties shown are statistical only. Fits to the data using Eq. (1), $C_{\text{inclusive}}(k^*)$, are displayed as solid lines, while the contribution $1 + x_{pp}\,[C_{pp}(k^*; R_{pp}) - 1]$ is indicated by dashed lines. The fit quality yields $\chi^2/\text{n.d.f.} = 1.66$ (1.61) for the top (middle) panel. In the proton–proton case, the scattering length f_0 and effective range d_0 are fixed to values obtained from elastic scattering measurements, namely $f_0 = 7.82$ fm and $d_0 = 2.78$ fm, reflecting the well-established nature of the p–p interaction. In contrast, for the antiproton–antiproton correlation, both f_0 and d_0 are treated as free parameters in the fit [24].

By fitting the measured correlation functions with the Lednický–Lyuboshitz model, the scattering length (f_0) and effective range (d_0) for the $\bar{p}$–$\bar{p}$ interaction were extracted, see Fig. 9. These parameters are consistent, within uncertainties, with those obtained for p–p. This result provides a quantitative confirmation of matter–antimatter symmetry in the strong interaction, demonstrating that the forces binding antinuclei are indistinguishable from those binding ordinary nuclear matter.

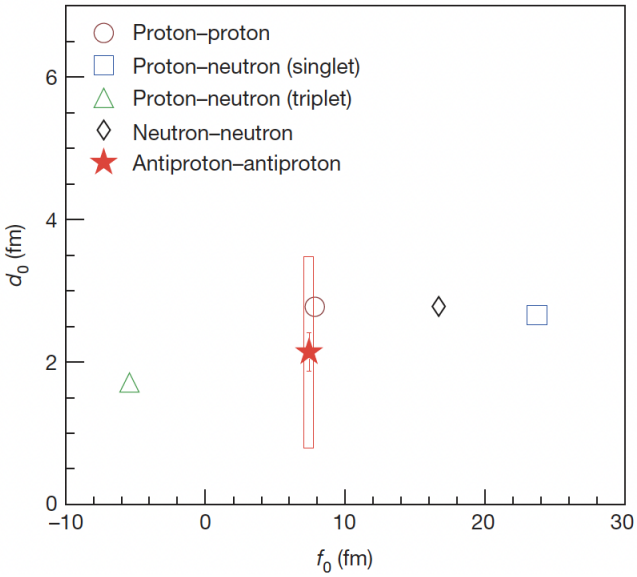

Fig. 9. The singlet s-wave scattering length (f_0) and effective range (d_0) for the antiproton–antiproton interaction are shown together with corresponding s-wave scattering parameters for other nucleon–nucleon systems. Statistical uncertainties are indicated by error bars, while the horizontal uncertainty on f_0 is smaller than the marker size. Systematic uncertainties are represented by shaded boxes. For the reference measurements, the uncertainties are of the order of a few percent and are smaller than the corresponding symbol sizes [24].

3.2. Hyperon–nucleon

The study of the p–Λ interaction is essential for understanding hyperon–nucleon (Y–N) forces, which play a key role in determining the properties of dense baryonic matter, including neutron stars. Femtoscopic measurements in p+Nb collisions at HADES offer a controlled environment for investigating these interactions.

The p–Λ correlation function presented in Fig. 10 is dominated by an attractive strong interaction, leading to a pronounced enhancement at low relative momentum. In small systems such as p+Nb, careful treatment of long-range correlations (LRC), induced by global conservation laws, is required. After accounting for these effects using transport-model baselines, the extracted p–Λ source is found to be slightly smaller than the p–p source, which may reflect differences in interaction cross sections and emission dynamics.

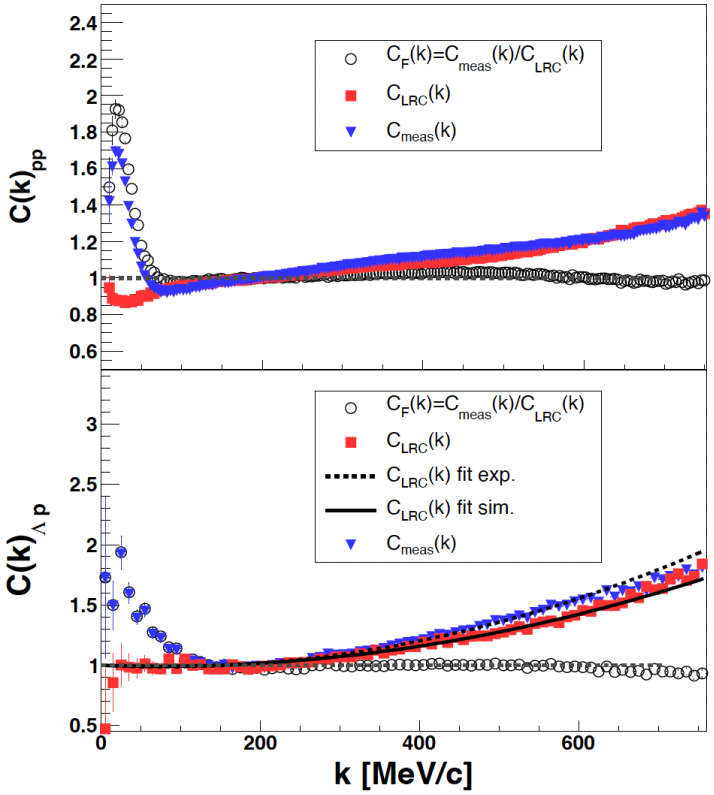

Fig. 10. Effects of long-range correlations (LRC) on the correlation functions for p–p pairs (top panel) and Λ–p pairs (bottom panel). Open circles represent the experimental correlation functions after correction for LRC. Blue triangles show the uncorrected experimental data including LRC, while red squares correspond to correlation functions obtained from transport model simulations. In the lower panel, the solid and dashed lines indicate polynomial fits to the simulated and experimental LRC contributions, respectively. See text for further details [25].

The sensitivity of the femtoscopic signal to the underlying hyperon–nucleon (Y–N) potential enables direct comparison with theoretical predictions from chiral effective field theory (χEFT). The data exhibit a clear dependence on the scattering length, with next-to-leading order (NLO) calculations providing a distinct description compared to leading-order (LO) results, see Fig. 11. This demonstrates that femtoscopy can serve as a powerful alternative to conventional scattering experiments, which are challenging for short-lived hyperons.

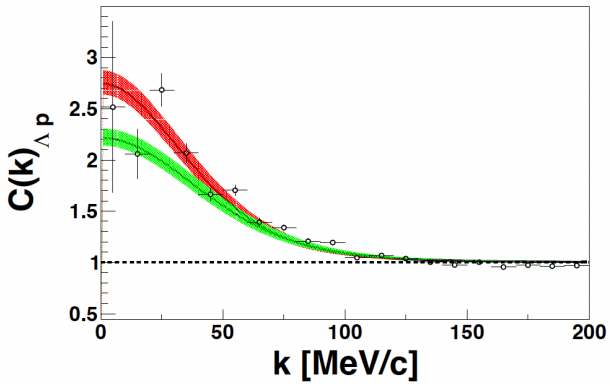

Fig. 11. Comparison of the experimental Λ–p correlation function (open circles with error bars) with the leading-order (LO, green) and next-to-leading-order (NLO, red) scattering parameter sets. The uncertainty bands on the theoretical curves reflect the uncertainties associated with the determination of the Λ–p source size [25].

3.3. Light nuclei

Extending femtoscopy to light nuclei, such as deuterons, provides access to three-body interactions and the mechanisms responsible for the formation of composite particles. In Au–Au collisions at $\sqrt{s_{NN}} = 3$ GeV, the STAR experiment has measured p–d and d–d correlation functions.

Both p–d and d–d systems exhibit a suppression at low relative momentum presented in Fig. 12, indicating an overall repulsive interaction. In the p–d case, this behavior is consistent with low-energy scattering data and theoretical expectations, where the doublet ($S = 1/2$) channel contains a bound state (^{3}He), while the quartet ($S = 3/2$) channel is repulsive. The extracted scattering parameters are in good agreement with existing experimental constraints.

The interpretation of these measurements is closely connected to the production mechanism of light nuclei. The observed agreement between the data and hadronic transport calculations employing a coalescence approach suggests that deuterons are predominantly formed via nucleon coalescence

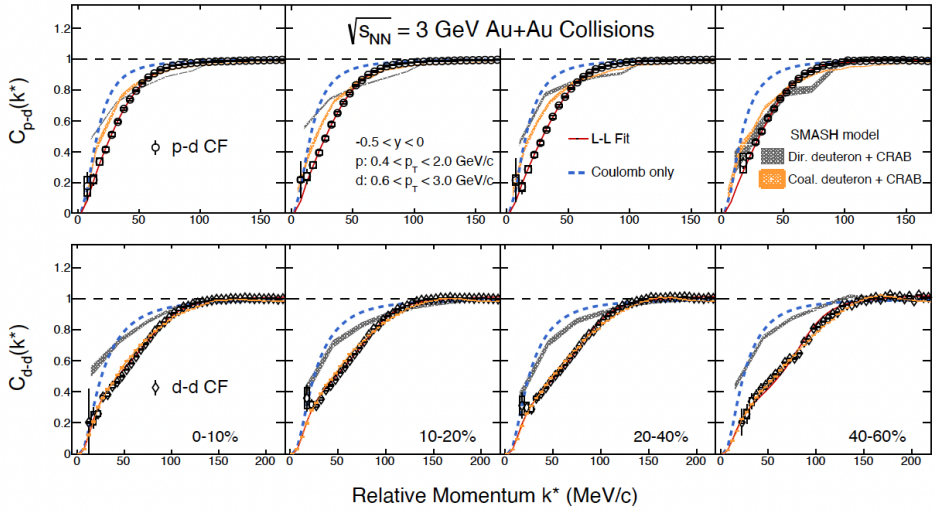

Fig. 12. Centrality dependence of the midrapidity correlation functions for p–d pairs (top panel) and d–d pairs (bottom panel), shown as a function of the relative momentum. Statistical uncertainties are indicated by error bars, while systematic uncertainties are represented by boxes. The results of the Lednický–Lyuboshits (LL) fits are shown as red lines. Orange bands correspond to calculations from the SMASH model combined with a coalescence procedure for deuteron formation followed by the CRAB afterburner, whereas gray bands represent model calculations with directly produced deuterons propagated through the CRAB afterburner. Blue dashed lines indicate results including only Coulomb interactions [26].

at kinetic freeze-out. Differences in the extracted Gaussian source radii for p–p, p–d, and d–d pairs can be understood in terms of m_{T} scaling, as heavier systems probe different regions of the expanding source. Sources sizes and extracted paramters of interactions are shown in Fig. 13.

3.4. Spin-separated states

A particularly advanced application of interaction femtoscopy is the extraction of spin-dependent interaction parameters. This is exemplified by studies of d–Λ correlations, where the pair can exist in either a spin-1/2 doublet (D) or a spin-3/2 quartet (Q) state.

The statistical weights of these configurations are fixed by quantum mechanics to 1/3 and 2/3, respectively. Using Bayesian inference techniques, it is possible to extract separate scattering lengths and effective ranges for the D and Q channels. The doublet channel is of special interest, as its interaction parameters are directly related to the binding energy of the hypertriton ($^{3}_{\Lambda}\mathrm{H}$).

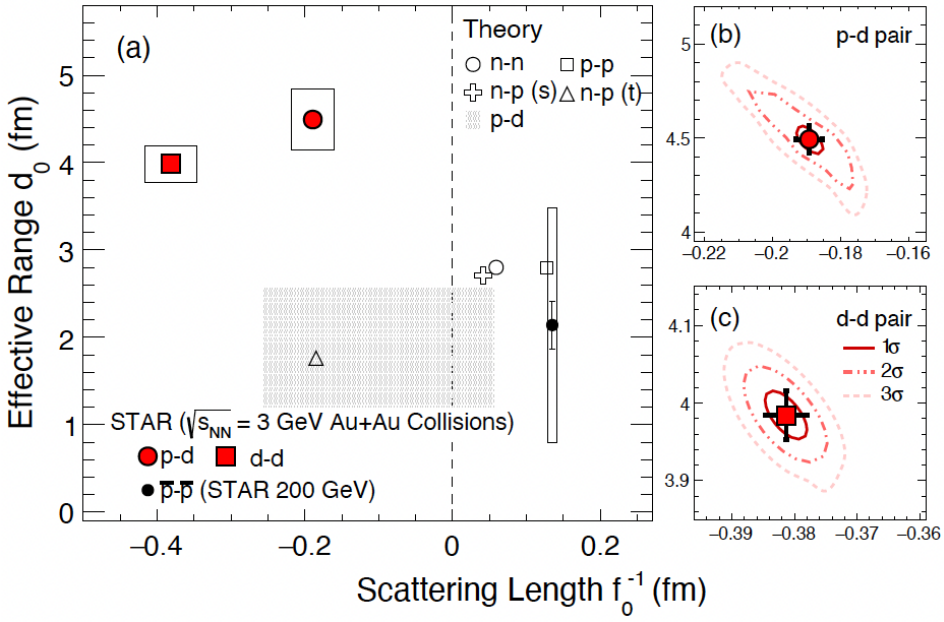

Fig. 13. (a) Spin-averaged final-state strong interaction parameters: the scattering length f_0 and the effective range d_0 extracted from p–d (filled circles) and d–d (filled squares) correlation functions. Statistical uncertainties are smaller than the marker size, while systematic uncertainties are indicated by open boxes. The result for the $\bar{p}$–$\bar{p}$ correlation function in 200 GeV Au+Au collisions is shown as the solid black point. Interaction parameters from n–n, p–p, n–p singlet (s) and triplet (t) states, as well as p–d interactions, are shown as open symbols and hatched regions. The 1–3σ confidence contours of the fit are displayed in the right panels (b) and (c) [26].

The analysis of correlation functions presented in Fig. 14 indicates a preference for a negative scattering length in the D channel, consistent with the existence of a weakly bound state. This enables an independent determination of the Λ separation energy (B_Λ) of the hypertriton. The extracted value agrees with the global average, demonstrating the reliability of the femtoscopic approach. Such spin-resolved studies provide the most detailed constraints to date on the d–Λ interaction and offer valuable insight into possible three-body forces involving hyperons in dense matter.

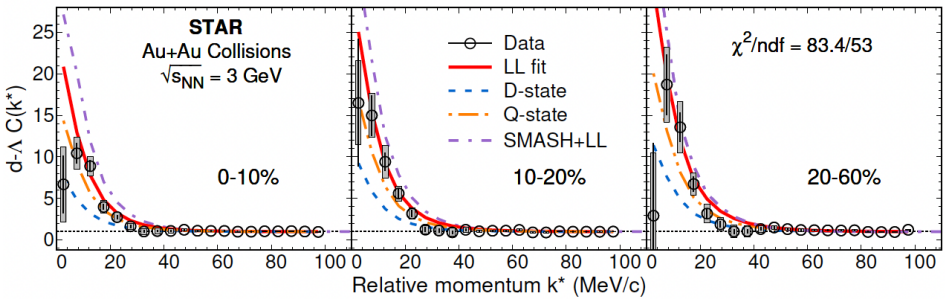

Fig. 14. The d–Λ correlation function $C(k^*)$ is shown as a function of the relative momentum k^* for different centrality classes. Statistical uncertainties are represented by error bars, while systematic uncertainties are indicated by boxes. Solid red lines correspond to constrained fits using the Lednický–Lyuboshits (LL) approach over the range 0–100 MeV/c. The combined fit quality for the three centralities is χ^2/n.d.f. = 83.4/53. Blue and orange dashed lines indicate the contributions from the D-state and Q-state, respectively, while the dashed purple line represents the SMASH+LL model calculations [27].

4. Summary

Femtoscopy has emerged as a powerful and versatile tool for probing both the collective dynamics of relativistic collisions and the fundamental interactions between hadrons. Systematic studies as a function of collision energy and system size reveal the development of collective flow and the evolution of the fireball from its initial anisotropic state to freeze-out. The observed scaling of homogeneity lengths with multiplicity and transverse momentum points to a common expansion mechanism in large systems, while emphasizing the role of initial geometry in smaller systems.

In the domain of interaction femtoscopy, the method has enabled the first direct measurements of the $\bar{p}$–$\bar{p}$ interaction, provided stringent constraints on hyperon–nucleon and light-nuclei interactions, and allowed for the separation of spin-dependent contributions. These results extend beyond purely geometric interpretations, supplying critical input for χEFT calculations and the equation of state of dense baryonic matter. With increasing experimental precision and the exploration of new collision systems, femtoscopy will continue to deepen our understanding of the space-time structure and microscopic dynamics of strongly interacting matter.

This work was supported by the grant of the National Science Centre (NCN), Poland, No. 2021/41/B/ST2/02409 and 2020/38/E/ST2/00019.

REFERENCES

[1] M. Lisa, S. Pratt, R. Soltz, U. Wiedemann, «Femtoscopy in Relativistic Heavy Ion Collisions: Two Decades of Progress», *Annu. Rev. Nucl.* **55**, 357 (2005).

[2] D.H. Boal, C.-K. Gelbke, B.K. Jennings, «Intensity interferometry in subatomic physics», *Rev. Mod. Phys.* **62**, 553 (1990).

[3] W. Bauer, C. Gelbke, S. Pratt, «Hadronic Interferometry in Heavy-Ion Collisions», *Annu. Rev. Nucl. Part. Sci.* **42**, 77 (1992).

[4] U. Heinz, B.V. Jacak, «Two-Particle Correlations in Relativistic Heavy-Ion Collisions», *Annu. Rev. Nucl. Part. Sci.* **49**, 529 (1999).

[5] U.A. Wiedemann, U. Heinz, «Particle interferometry for relativistic heavy-ion collisions», *Phys. Rep.* **319**, 145 (1999).

[6] R. Hanbury-Brown, R.Q. Twiss, «A Test of a New Type of Stellar Interferometer on Sirius», *Nature* **178**, 1046 (1956).

[7] R. Hanbury-Brown, R.Q. Twiss, «LXXIV. A new type of interferometer for use in radio astronomy», *Philos. Mag.* **45**, 663 (1954).

[8] G. Kopylov, M. Podgoretsky, «Correlations of identical particles emitted by highly excited nuclei», *Sov. J. Nucl. Phys.* **15**, 219 (1972).

[9] G. Kopylov, V. Lyuboshits, M. Podgoretsky, JINR-P2-8069.

[10] G. Kopylov, M. Podgoretsky, «Multiple production and interference of particles emitted by moving sources», *Sov. J. Nucl. Phys.* **18**, 336 (1974).

[11] S. Pratt, «Pion interferometry of quark–gluon plasma», *Phys. Rev. D* **33**, 1314 (1986).

[12] Q.H. Zhang, U.A. Wiedemann, C. Slotta, U. Heinz, «Bose–Einstein weights for event generators», *Phys. Lett. B* **407**, 33 (1997).

[13] U.A. Wiedemann *et al.*, «Quantum mechanical localization effects for Bose–Einstein correlations», *Phys. Rev. C* **56**, R614 (1997).

[14] U.A. Wiedemann, D. Ferenc, U. Heinz, «Coulomb final state interactions for Gaussian wave packets», *Phys. Lett. B* **449**, 347 (1999).

[15] M. Gyulassy, Iu. Karpenko, A.V. Nazarenko, Yu.M. Sinyukov, «HBT and initial conditions for hydrodynamic expansion in A+A collisions», *Braz. J. Phys.* **37**, 1031 (2007).

[16] A.N. Makhlin, Yu.M. Sinyukov, «The hydrodynamics of hadron matter under a pion interferometric microscope», *Z. Phys. C* **39**, 69 (1988).

[17] S. Pratt, «Validity of the smoothness assumption for calculating two-boson correlations in high-energy collisions», *Phys. Rev. C* **56**, 1095 (1997).

[18] S.E. Koonin, «Proton pictures of high-energy nuclear collisions», *Phys. Lett. B* **70**, 43 (1977).

[19] G.F. Bertsch, «Pion interferometry as a probe of the plasma», *Nucl. Phys. A* **498**, 173 (1989).

[20] HADES Collaboration (J. Adamczewski-Musch *et al.*), «Identical pion intensity interferometry at $\sqrt{s_{NN}} = 2.4$ GeV», *Eur. Phys. J. A* **56**, 140 (2020).

[21] STAR Collaboration (L. Adamczyk *et al.*), «Beam-energy-dependent two-pion interferometry and the freeze-out eccentricity of pions measured in heavy ion collisions at the STAR detector», *Phys. Rev. C* **92**, 014904 (2015).

[22] STAR Collaboration (J. Adam *et al.*), «Two-pion femtoscopy in p–Pb collisions at $\sqrt{s_{NN}} = 5.02$ TeV», *Phys. Rev. C* **91**, 034906 (2015).

[23] STAR Collaboration (J. Adams *et al.*), «Pion–Kaon Correlations in Central Au+Au Collisions at $\sqrt{s_{NN}} = 130$ GeV», *Phys. Rev. Lett.* **91**, 262302 (2003).

[24] STAR Collaboration, «Measurement of interaction between antiprotons», *Nature* **527**, 345 (2015).

[25] HADES Collaboration (J. Adamczewski-Musch *et al.*), «Λp interaction studied via femtoscopy in p+Nb reactions at $\sqrt{s_{NN}} = 3.18$ GeV», *Phys. Rev. C* **94**, 025201 (2016).

[26] STAR Collaboration, «Light nuclei femtoscopy and baryon interactions in 3 GeV Au+Au collisions at RHIC», *Phys. Lett. B.* **864**, 139412 (2025).

[27] STAR Collaboration, «First observation of deuteron–Λ correlations at RHIC», arXiv:2511.15493 [nucl-ex].